Co_3O_4 Hollow Nanospheres Doped with $ZnCo_2O_4$ via Thermal Vapor Mechanism for Fast Lithium Storage

ABSTRACT: Binary metal oxides offer improved anode materials in lithium ion batteries owing to enhanced electrical conductivity but suffer from large volume expansion on lithiation. A novel route to hollow Co_3O_4 nanospheres doped with $ZnCo_2O_4$ is demonstrated that mitigates the expansion issue and shows excellent performance at high current densities. The synthetic route is based on the pyrolysis of binary metal-organic-frameworks (MOFs) with the controlled loss of zinc tuning the micro and nanostructure of the material through a thermal vapor mechanism. The optimal structures, that contain hollow Co_3O_4 spheres of ca. 50 nm diameter doped with $ZnCo_2O_4$, show a specific capacity of 890 mAh g^{-1} at a current rate of 0.1 A g^{-1} and show a similar specific capacity at 1 A g^{-1} after 120 cycles at high current densities. The kinetics of lithiation/delithiation changes from diffusion-controlled to a surface-controlled process by the nanosizing of the particles. The resultant faster ion diffusion and capacitive storage for lithium ions are responsible for the extraordinary high-rate performance of the hollow structures.

KEYWORDS: binary metal oxide doping, metal organic frameworks, thermal vapor transport mechanism, lithium storage

Graphic abstract

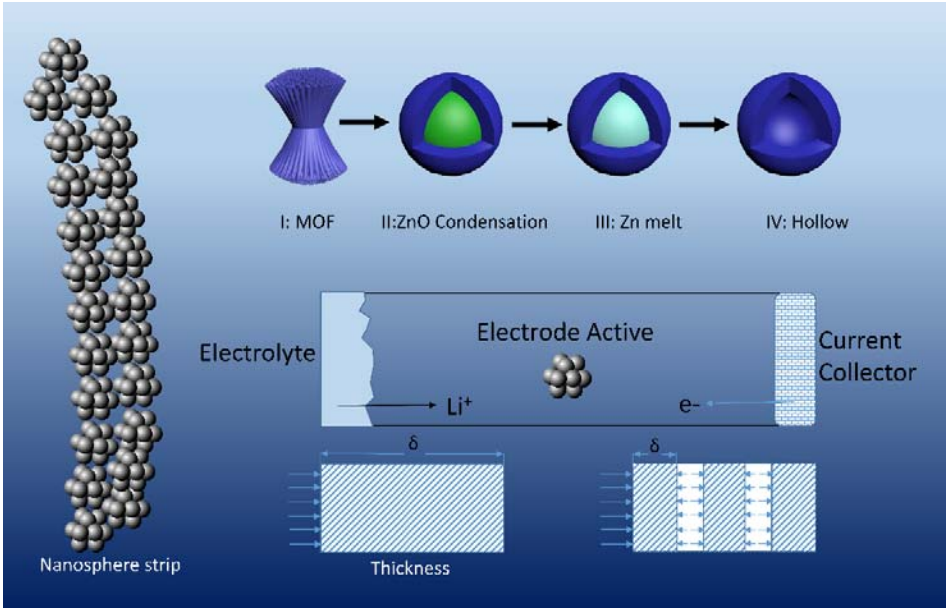

Hollow Co_3O_4 nanospheres doped with $ZnCo_2O_4$ is prepared from the pyrolysis of binary metal-organic-frameworks (MOFs) with the controlled loss of zinc tuning the micro and nanostructure of the material through a thermal vapor transport mechanism.

1. Introduction

Development of novel electrode materials has led to improvements in the performance of Lithium Ion Batteries (LIBs) since they were first commercialized by Sony in 1991. It is generally accepted that higher energy and power densities will be achieved by improvements in the anode materials[1-3]. Anodes of transition metal oxides such as Co_3O_4 offer higher theoretical specific capacities, 890 mAh g^{-1} (Co_3O_4+8Li→ 3Co + 4Li_2O) than commonly employed commercial graphite, 372 mAh g^{-1} (6C+Li→LiC_6)[4, 5]. Whilst Co_3O_4 offers high specific capacity, it has not been adopted as a material of choice for LiB anodes owing to its poor electrical conductivity and high volume change upon lithiation[6], 249% for Co_3O_4.

Mixed transition metal oxides, $A_xB_{3-x}O_4$, can lead to improved conductivity, owing to facile electron hopping between the multivalent metal centres, and hence improved material performance[7-9]. Such doping of transition metal oxides for improved conductivity is preferred because the material is also capable of lithium storage. Of the mixed transition metal oxides containing cobalt oxide, available $ZnCo_2O_4$ offers the greatest potential capacity in an LIB as the Zn formed in the conversion reaction, $ZnCo_2O_4$ + 8Li → Zn + 2Co + 4Li_2O, can alloy with lithium to yield $ZnLi_{x[1]}$. However, bulk $ZnCo_2O_4$ also suffers large volume variation of 211% on lithiation/delithiation. Expansion of the metal oxides upon lithiation leads to electrode pulverization and loss of contact with the current collector upon repeated cycling[10]. The use of nanomaterials, which are able to better accommodate the material swelling can lead to anodes with improved cyclability[11-14]. Another way to reduce the problem of swelling is to form micro/nano-structures or composite with carbon-based materials, that can buffer the volume change from both sides of the phases[15-19]. Mesoporous $ZnCo_2O_4$ microspheres composed of nanoparticles have been reported[20] to exhibit an initial specific capacity of 937 mAh g^{-1} and retain 432 mAh g^{-1} after 40 cycles at a current rate of 1 A g^{-1}. Ultrathin $ZnCo_2O_4$ nanosheets[21] grown on reduced graphene oxide have shown very stabe reversible capacity around 960 mAh g^{-1} at 90 mA g^{-1}. Metal-organic-frameworks (MOFs) derived

$ZnCo_2O_4$ porous hollow spheres coated with Ag via a Ag-mirror reaction[22] exhibited a high reversible capacity of 616 mA h g^{-1} after 900 cycles at 1 A g^{-1} and excellent capacity retention at high rate of 20 A g^{-1}. The prepared carbon nanofibers anchored with $Zn_xCo_{3-x}O_4$ nanocubes by hydrothermal and thermal treatment delivered a high capacity of 600 mAh g^{-1} and excellent cycling stability[23]. The tuning of the composition of the material is proposed to influence the theoretical capacity and cycling properties in a lithium-ion battery.

The pyrolysis of MOFs has been a popular technique for the preparation of metal oxide nanocomposites[11, 24-29]. A MOF is formed by organic ligands connecting metal centers and changes in ligand type, coordination of the metal clusters, reaction time, ligand-to-metal ion ratios, solvent and temperature alter the MOF framework as well as its physicochemical properties[30, 31]. The microstructure of the metal oxide composite formed on pyrolysis of the MOF depends on that of the parent MOF and the conditions of pyrolysis.

Herein a novel route, namely thermal vapor method to the formation of hollow Co_3O_4 doped with $ZnCo_2O_4$ via the pyrolysis of a mixed-ion ZnCo MOF is investigated. The influence of synthesis conditions on the structure of both the MOF and the pyrolyzed composite are discussed. In the pyrolysis of the ZnCo MOFs, ZnO is condensed in the center of a particle and then reduced by a thermal vapor mechanism in the reductive condition. The controllable loss of Zn by the thermal vapor results in the formation of hollow sphere. The doping level of $ZnCo_2O_4$ in the hollow structure is tuned by the loss of Zn and the optimal resultant hollow structures doped with low amounts of $ZnCo_2O_4$ show very high specific capacity and excellent cyclability as the anode materials in lithium-ion batteries.

2. Experimental

2.1 Synthesis of mixed-ion ZnCo MOFs: All chemicals were sourced from Sigma-Aldrich and used without any further processing. In a synthesis, 4 mmol $Zn(NO_3)_2.6H_2O$ (1.19 g), 8 mmol $CoCl_2.6H_2O$ (1.9 g) and a defined number of moles of terephthalic acid were added to a mixture of dimethylacetamide (DMA, 50 mL) and

methanol (30 mL). 1.5 g polyvinylpyrrolidone (PVP) powder (average Mw ~55,000) was added to the solution and the system was stirred for 60 minutes. The mixture obtained was transferred to a 125 mL autoclave and kept at 150 ^{o}C for a set period. After washing with DMA and methanol the precipitate was recovered by centrifugation and dried in vacuum at 80 ^{o}C. Six different batches of ZnCo MOFs were prepared defined by the amount, in mmol, of terephthalic acid ligand used in the synthesis and the time in h of the solvothermal reaction; ZnCoMOF(1.3 mmol, 12 h), ZnCoMOF(3.5 mmol, 3 h), ZnCoMOF(3.5 mmol, 8 h), ZnCoMOF(3.5 mmol, 12 h), ZnCoMOF(3.5 mmol, 14 h) and ZnCoMOF(3.5 mmol, 16 h).

2.2 Synthesis of $Co_3O_4/ZnCo_2O_4$ composites: The ZnCoMOFs were pyrolized in Ar, samples were heated to 550 ^{o}C, the temperature was maintained for 2 h and then the system was cooled back to room temperature. Two heating rates were employed in the pyrolysis 10 and 2 ^{o}C min^{-1}. Finally the samples were calcined in air at 350 ^{o}C for 2 h. Samples are labelled ZCO(*x* mmol, *y* h, *z*) where *x* and y are the number of mmol of terephthalic acid ligand used and the length of heating in the autoclave during the synthesis of the parent MOF respectively and *z* is the heat rate employed in the pyrolysis.

2.3 Material Characterization: The crystallographic structure of the as-prepared materials was studied by X-ray powder diffraction (XRD) using a Bruker D8 diffractometer with monochromatic Cu Kα radiation (λ=1.5406 Å), and the diffraction data was recorded in the 2θ range of 10–80 ^{o}. Scanning electron microscopy (SEM) images were recorded on LEO Gemini 1525 FEG. Transmission electron microscopy (TEM) images, selected area electron diffraction (SAED) and scanning transmission electron microscopy (STEM) were carried out on JEM 2100F. X-ray photoelectron spectroscopy (XPS) was measured using a Thermo Scientific K-Alpha instrument. The thermogravimetric analysis/differential scanning calorimetry (TGA/DSC) of the samples was carried out on a Diamond TG thermo-analyzer. Inductively coupled plasma optical emission spectrometry (ICP-OES) was carried out on a iCAP 6000 Series ICP Spectrometer from Thermo Scientific.

2.4 Simulation: Molecular structure and simulation was fabricated using ChemDraw 16.0 and Chem3D 16.0 software. The optimized molecular structure was deduced using

MM2 force-field theory and molecular orbital was simulated using the extended Huckel method.

2.5 Electrochemical tests: The as-prepared materials were mixed with acetylene black and binder (sodium carboxymethyl cellulose, CMC) in a weight ratio of 7:2:1 using distilled water as solvent. The solution was placed on a copper foil as current collector and the electrode dried in a vacuum oven at 100 ^{o}C for 24 h. R2032 coin cells were assembled in an argon-filled glove box using metallic lithium as the cathode and Celgard 2500 membrane as separator. The electrolyte was 1 M $LiPF_6$ dissolved in a mixture of ethylene carbonate (EC) anddimethyl carbonate (DMC) (v/v, 1/1). Cyclic voltammetry (CV) and galvanostatic charge/discharge cycling tests were carried out over a set voltage range using an Autolab workstation (GPES software) and a 580 Bycycle battery test system, respectively. Electrochemical impedance spectroscopy (EIS) was studied using a Solartron Analytical 1286 Interface and 1260 Frequency Response Analyser, an ac amplitude of 5 mV in the frequency range from 1000 Hz to 10 mHz was employed. All electrochemical tests were carried out at room temperature.

3. Results and Discussion

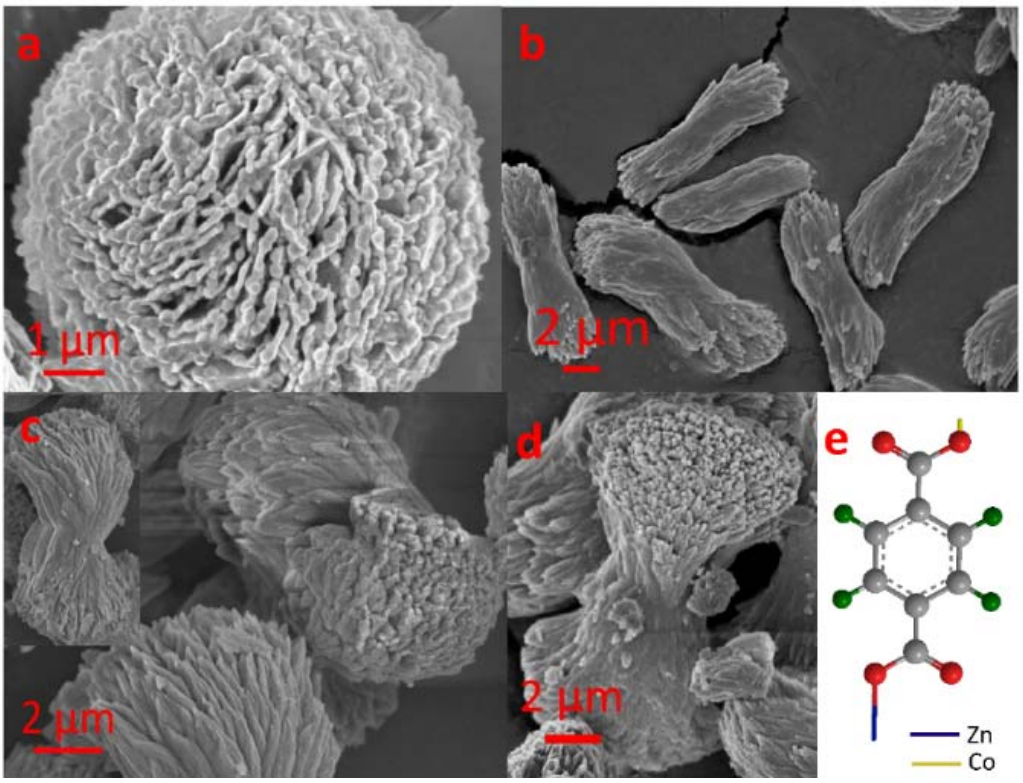

Figure 1. SEM images of ZnCoMOF prepared via the solvothermal method. MOF from the precursor (a) using 1.3mmol H_2BDC with 12h solvothermal reaction, and using 3.5mmol H_2BDC with (b) 12h, (c) 14h and (d) 16h reaction time. (e) Bond length between the metal ions (blue bond is zinc and yellow is cobalt) and the organic ligand, H_2BDC, spheres in grey, green and red denote carbon, hydrogen and oxygen atoms respectively.

Mixed-ion ZnCoMOFs were synthesized by a solvothermal reaction in a mixture of dimethylacetamide (DMA, 50mL) and methanol (30mL) at 150 ^oC using $CoCl_2$ and $Zn(NO_3)_2$ as metal ion sources and terephthalic acid (H_2BDC) as ligand. **Figure 1** and S1 show the morphology at the micron scale of the as-prepared ZnCoMOFs. When 1.3 mmol H_2BDC is added to the Co and Zn precursors and a reaction time of 12 hours employed, the resultant porous ZnCoMOF(1.3mmol, 12h) is spherical in microstructure (Figures 1a and S1a). Increasing the amount of H_2BDC to 3.5 mmol and maintaining a reaction time of 12 h, ZnCoMOF(3.5mmol, 12h), results in a change of microstructure, from spherical to dumbbell shaped

(Figure 1b). At longer reaction times, ZnCoMOF(3.5mmol, 14h) and ZnCoMOF(3.5mmol, 16h), the heads of the dumbbells expand (figures 1c and 1d) whilst at shorter reaction times, ZnCoMOF(3.5mmol, 3h) and ZnCoMOF(3.5mmol, 8h), mixtures of spheres and dumbbells are observed (Figures S1b and S1c). X-ray diffraction (XRD) patterns for the MOFs prepared using 3.5 mmol H_2BDC at different reaction times (Figure S2) show an evolution in crystal structure with increasing reaction time[30] and shows different crystal structure in comparison with tetragonal MOF-5. The high-resolution X-ray Photoelectron Spectra (XPS) of Co $2p_{3/2}$ and Zn 2p of ZnCoMOF(3.5mmol, 3, 8, 12 and 16h) are displayed in Figure S3. All the samples show approaching fitted peaks in both Co $2p_{3/2}$ and Zn $2p_{3/2}$ which are around 781 and 1022 eV, indicating the existence of Co(II)[32] and Zn(II)[11] in the metal-oxygen bond. The Co:Zn ratios in the six prepared, MOFs determined using inductively coupled plasma optical emission spectrometry (ICP-OES, Table S1), indicate that the 2:1 elemental ratio employed in the synthesis is not maintained in the product. In all cases the ratio of Co:Zn is greater than 2 indicating Co^{2+} incorporation is preferred. The bonding of Co^{2+} and Zn^{2+} ions with H_2BDC results in Co-O and Zn-O bonds. Co-O has a shorter bond length (0.6 Å) than Zn-O (1.89 Å), see Figure 1e. The stronger Co-O interaction than Zn-O interaction, see the molecular orbitals (Figure S4), results in the preferable incorporation of Co^{2+}. The binding energy of Co-O and Zn-O is not influened by the different ratio of Co:Zn in the ZnCoMOFs, as indicated by the XPS analysis. Comparison of the Co:Zn ratios in ZnCoMOF (1.3mmol, 12h) and ZnCoMOF (3.5mmol, 12h), 13.4 and 4.4 respectively, indicate that the higher ligand concentration results in an increase in Zn^{2+} uptake. The amount of Zn^{2+} in the product is found to increase with reaction time, see Table S1. The reaction between 3.5mmol H_2BDC and Co^{2+} ions in the absence of Zn^{2+} ions for 12h produces a non-uniform MOF structure, as shown in Figure S5.

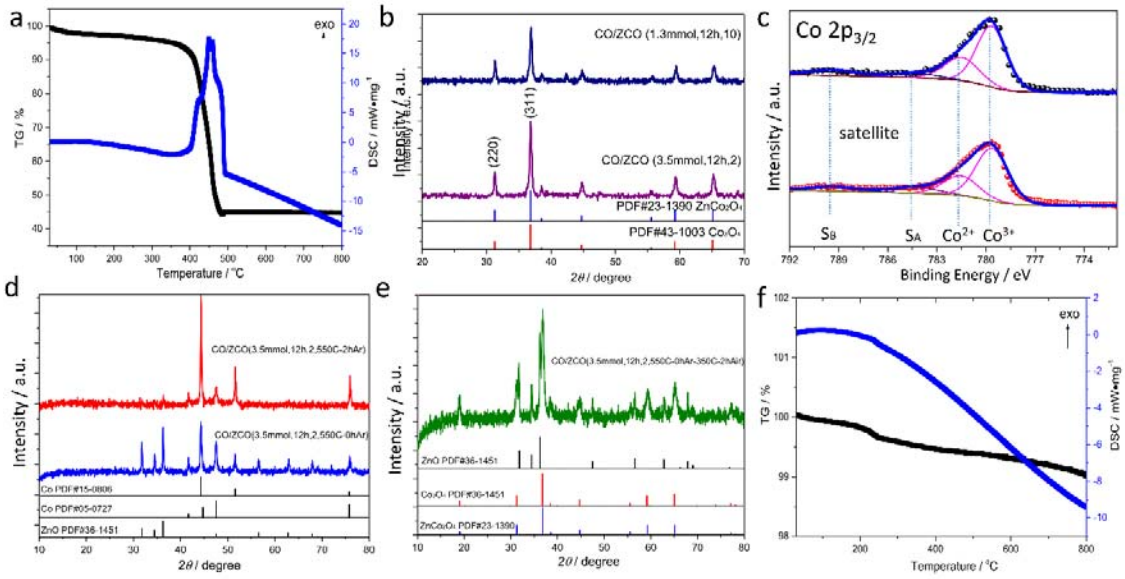

Figure 2. Characterization of $Co_3O_4/ZnCo_2O_4$ from ZnCoMOFs at specific decomposition rates. (a) TGA/DSC curves of ZnCoMOF (3.5mmol, 12h) in an inert atmosphere. (b) XRD patterns of CO/ZCO (1.3mmol, 12h, 10) and CO/ZCO (3.5mmol, 12h, 2) pyrolised from the corresponding MOFs. The number in mmol is the amount of H_2BDC, the number in h is the reaction time for MOF growth and the last number is the decomposition rate in Ar. (c) High resolution XPS of Co $2p_{3/2}$ in CO/ZCO (1.3mmol, 12h, 10) (upper pattern) and CO/ZCO (3.5mmol, 12h, 2). (d) XRD patterns of the products after the pyrolysis of CO/ZCO (3.5mmol, 12h) at 550 ^oC in Ar for 0h, CO/ZCO (3.5mmol, 12h, 2, 550C-0hAr) and 2 h, CO/ZCO (3.5mmol, 12h, 2, 550C-2hAr). (e) XRD of CO/ZCO (3.5mmol, 12h, 2, 550C-0hAr) annealed in air for 2h, CO/ZCO (3.5mmol, 12h, 2, 550C-0hAr-350C-2hAir). (f) TGA/DSC curves of CO/ZCO (3.5mmol, 12h, 2) in the air.

Metal oxide nanocomposites were prepared by decomposition of the as-prepared ZnCoMOFs in Ar at 550 ^oC for 2 hours. Thermogravimetry and differential scanning calorimetry (TGA/DSC) curves of ZnCoMOF (3.5mmol, 12h) in an inert atmosphere show the collapse of the MOF skeleton at *ca.* 500 ^oC, see **Figure 2**a. The samples were then subject to calcination in air at 350 ^oC for 2 hours. XRD

patterns of the pyrolysed ZnCoMOFs are shown in Figure 2b, diffractograms are displayed for materials in which two different heating/cooling rates in Ar were employed, 2 and 10 ^{o}C min^{-1}. All materials formed by pyrolysis of the ZnCoMOFs show cubic crystal structures consistent with the diffraction patterns of both Co_3O_4 and $ZnCo_2O_4$ and there is no evidence of any ZnO or Zn phase. Given the Co:Zn ratio in the parent MOFs and in the pyrolyzed materials is greater than 2:1 it appears that the product contains both Co_3O_4 and $ZnCo_2O_4$. The mixed Co_3O_4:$ZnCo_2O_4$ materials formed are designated CO/ZCO (*x*mmol, *y*h, *z*) where *x* and *y* refer to the concentration of ligand and the time in the autoclave for generation of the parent MOF and *z* is the heat rate used in the pyrolysis step. Chemical analysis of the products using Energy Dispersive X-ray Spectroscopy (EDX) and ICP-OES indicates that the resultant materials contain Co and Zn with the Co always in excess (Figure S6 and Table S2).

The high-resolution XPS of Co $2p_{3/2}$ of CO/ZCO (3.5mmol, 12h, 2) and CO/ZCO (1.3mmol, 12h, 10) are shown in Figure 2c. The surface Co $2p_{3/2}$ spectra show two distinct peaks at binding energies of 779.6 and 781.5 eV with small satellite peaks (S_A and S_B), indicating the existence of Co(III) and Co(II)[32]. The fitted spctra quantify the atomic ratios of Co(III):Co(II) in CO/ZCO (3.5mmol, 12h, 2) and CO/ZCO (1.3mmol, 12h, 10) are 2.4 and 2.2. The ratio above 2 indicates $ZnCo_2O_4$ is in the composite with small amount and the higher ratio of 2.4 means a higher content of $ZnCo_2O_4$ in CO/ZCO (3.5mmol, 12h, 2) than CO/ZCO (1.3mmol, 12h, 10), consistent with the ICP results in Table S2. The depth profiles[33] of Co and Zn in the composite is presented in Figure S7 which was etched with Ar^+ ions from the Ar gun in XPS instrument at a rate around 0.2 nm s^{-1}. Zn 2p spectra display a doublet but the noisy signal indicates the content of Zn in both surface and bulk is low, again resulting from the small amount of $ZnCo_2O_4$. Co $2p_{3/2}$ spectra show little shift in position and intensity with increased etching time but the satellite peaks are enhanced, indicating the Co(III) might be reduced by the etching ions

To investigate the reason of the low content of Zn in the pyrolyzed products relative to the parent MOFs, experiments were performed using different heating regimes. ZnCoMOF(3.5mmol, 12h) was heated at 2 ^{o}C min^{-1} in an Ar atmosphere to a temperature of 550 ^{o}C and either immediately cooled, CO/ZCO(3.5mmol, 12h, 2, 550C-0hAr) or kept at 550 ^{o}C for 2 h prior to cooling, CO/ZCO(3.5mmol, 12h, 2, 550C-2hAr). XRD analysis of CO/ZCO(3.5mmol, 12h, 2, 550C-0hAr) shows ZnO crystals of 39.2nm, as determined using the Scherrer equation along the (101) direction, are formed, see Figure 2d. Holding the sample at 550^{o}C for 2h extends the reduction of ZnO to Zn and the temperature above the melting point of nanosized Zn (419^{o}C) causes the loss of Zn via a thermal vapor mechanism[34]. The loss of Zn is confirmed by the Co:Zn ratios of CO/ZCO(3.5mmol, 12h, 2, 550C-0hAr) and CO/ZCO(3.5mmol, 12h, 2, 550C-2hAr) being 3.3 and 18.4 from ICP, as listed in Table S2. The loss of Zn is promoted by the reductive reagents[35-37], such as carbon and transition metal, Co, yielded from the heating of ZnCoMOF(3.5mmol, 12h) in Ar at 550^{o}C for 2 h[38], see diffractogram in Figure 2d, which is in line with the reported conclusion[39].

Thus, the holding time at 550^{o}C in Ar controls the amount of ZnO left in the pyrolysis intermediate and determines the amount of $ZnCo_2O_4$ dopant in the product. The annealing of CO/ZCO (3.5mmol, 12h, 2, 550C-0hAr) and CO/ZCO (3.5mmol, 12h, 2, 550C-2hAr) in the air at 350 ^{o}C for 2 h oxidizes the Co to Co_3O_4 and triggers the reaction with ZnO. XRD of the product, CO/ZCO (3.5mmol, 12h, 2, 550C-0hAr-350C-2hAir) in Figure 2e shows that the patterns match Co_3O_4/$ZnCo_2O_4$ and ZnO while there is no ZnO pattern in CO/ZCO (3.5mmol, 12h, 2), see Figure 2b. The excess ZnO from the Co/ZnO intermediate is not able to react with the oxidized Co_3O_4 to become $ZnCo_2O_4$ because the formation of a solid solution from the ZnO-Co_3O_4-$ZnCo_2O_4$ system needs higher energy that is unavailable at 350^{o}C[40]. Also, the large ZnO particles in the intermediate, CO/ZCO(3.5mmol, 12h, 2, 550C-0hAr) may lose contact with the Co particles further reducing the probability of reaction. The annealing of ZnCoMOF (3.5mmol, 12h) at 350^{o}C in the air for 2h burns off the carbon framework and results in crystal CO/ZCO (3.5mmol, 12h, 2, 350-2hAir) with a Co:Zn ratio of 3.3,

denoting the high content of $ZnCo_2O_4$ in the composite, see Figure S8 and Table S2.

Scherrer equation analysis of the (311) peak in the XRD patterns, Figure 2b, for CO/ZCO (1.3mmol, 12h, 10) and CO/ZCO (3.5mmol, 12h, 2) yields a primary crystallite of *ca.* 24.6 nm for both nanomaterial samples. Standard powder diffraction patterns for Co_3O_4 and $ZnCo_2O_4$ show intensity ratios for the (220):(311) peaks of 0.33 and 0.35, respectively; whilst for CO/ZCO (1.3mmol, 12h, 10) and CO/ZCO (3.5mmol, 12h, 2) the ratios of the peaks are 0.83 and 0.53, which is consistent with preferred crystal growth perpendicular to the (220) plane. Thermal analysis of the as-prepared materials, Figure 2f, points to there being less than 1% carbon in the final product. Nitrogen (N_2) absorption/desorption isotherms of CO/ZCO (3.5mmol, 12h, 2) and CO/ZCO (3.5mmol, 16h, 2), Figure S9, analysed using the Brunauer-Emmett-Teller (BET) method indicate that the materials have surface areas of 47 and 57 $m^2 g^{-1}$ respectively. Analysis using Density Functional Theory (DFT) shows that the two samples have similar pore size distributions, centered below 5 nm, indicating that the transition metal oxide nanomaterials formed have both micro- and meso-pore characteristics, Figure S10.

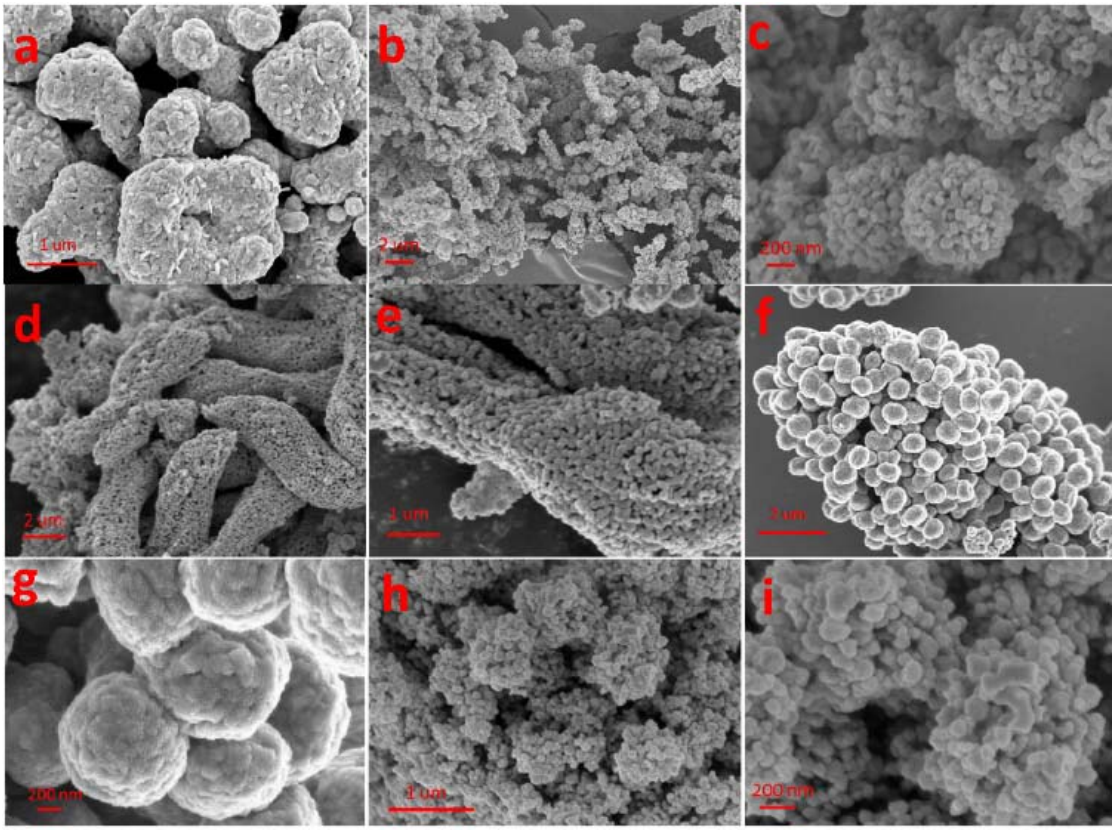

Figure 3. FESEM images of CO/ZCO decomposed from ZnCoMOF at (a-e) 2 ^{o}C min^{-1} and (f-i) 10 ^{o}C min^{-1}. CO/ZCO (*x* mmol, *y* h, *z*) where *x* and *y* refer to the concentration of ligand and the time in the autoclave for generation of the parent MOF and *z* is the heat rate used in the pyrolysis step. (a) CO/ZCO (1.3mmol,12h,2), (b, c) CO/ZCO (3.5mmol,12h,2), (d, e) CO/ZCO (3.5mmol,16h,2), (f, g) CO/ZCO (1.3mmol,12h,10), (h, i) CO/ZCO (3.5mmol,12h,10).

Field-emission scanning electron microscopy (FESEM) images show the morphology of CO/ZCO formed from the ZnCoMOFs, **Figure 3**. Samples prepared via slow heating, 2 ^{o}C min^{-1} of the MOF in an inert atmosphere retain the structure of the parent MOF, Figures 3(a-e). When a higher heating rate is used for the pyrolysis, 10 ^{o}C min^{-1}, the microstructure of the parent MOF is lost, Figures 3 (f-i), and the system becomes an amalgamation of spheres. The similar morphology change is also observed for CO/ZCO (3.5mmol,3h,2), CO/ZCO

(3.5mmol,3h,10), CO/ZCO (3.5mmol,8h,2) and CO/ZCO (3.5mmol,8h,2) which are resulted from the MOFs with different hydrothermal time, see Figure S11. When a low concentration of ligand is employed in preparing the initial MOF, the spheres are rough and greater than 1 μm in diameter, whilst when a higher ligand concentration is employed in synthesizing the parent MOF the spheres in the CO/ZCO composite are less than 200 nm in diameter.

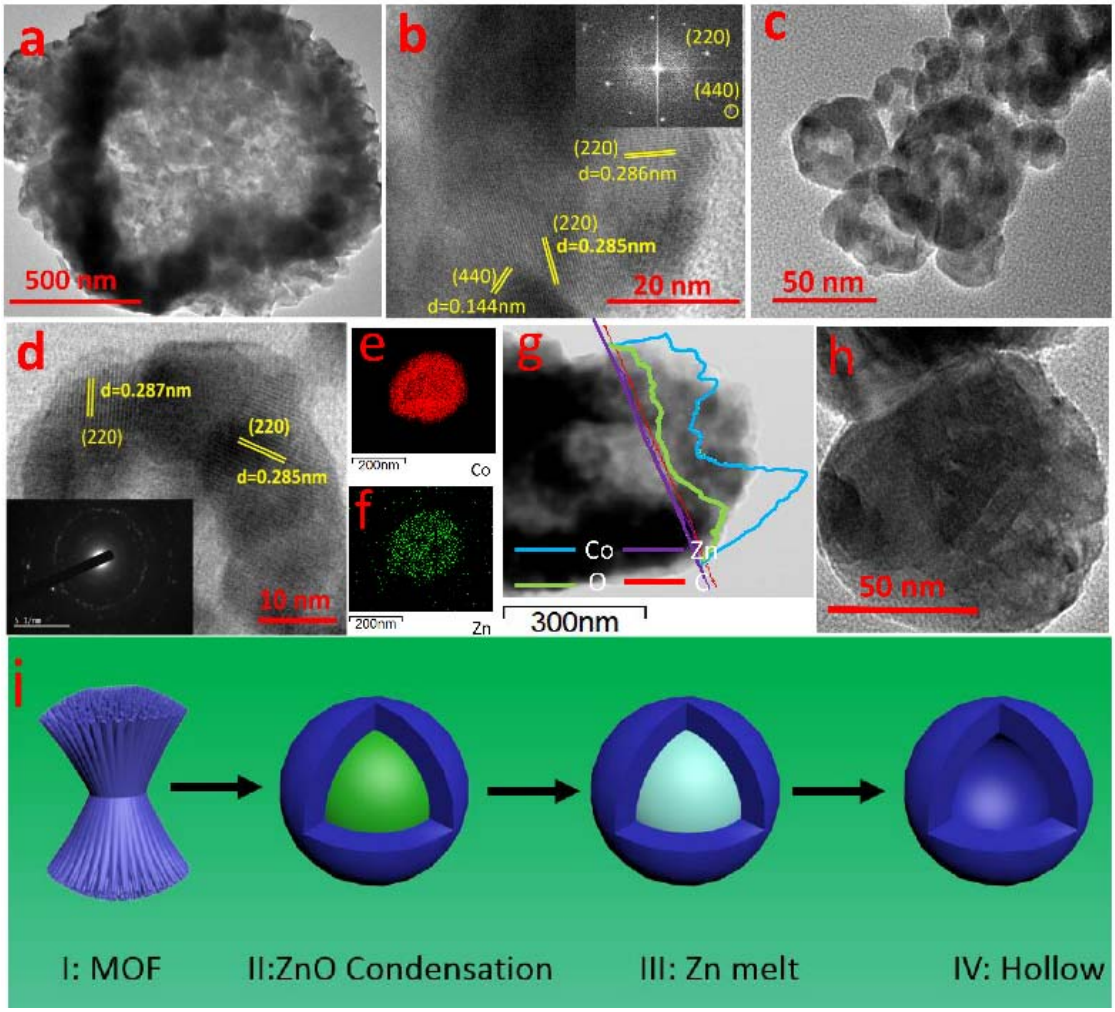

Figure 4. TEM and HRTEM images of (a, b) CO/ZCO (1.3mmol, 12h, 10) and (c, d) CO/ZCO (3.5mmol, 12h, 2). The inset in (b) is the FFT of the selected HRTEM area and in (d) is the SAED. (e, f) Elemental mapping of Co and Zn. Line scan mapping of (g) CO/ZCO (1.3mmol, 12h, 10). (h) TEM image of a sphere of CO/ZCO (3.5mmol, 12h, 2, 550-0hAr-350-2hAir). (i) Schematic representation of the formation process of the hollow structure. I: ZnCo MOFs growth; II: ZnO

condensation to the middle of the pyrolyzed particle; III: Zn reduction and melt from the middle; IV: Hollow CO doped with ZCO after losing Zn.

Transition electron microscopy (TEM) images of CO/ZCO (1.3mmol, 12h, 10) and CO/ZCO (3.5mmol, 12h, 2) indicate the micro- and nano-spheres formed on pyrolysis are hollow, **Figures 4**(a) and (c), formed with crystals in dimension of 20-30 nm, consistent with the XRD data. The High Resolution TEM (HRTEM) image of the larger spheres, Figure 4(b), shows lattice fringes consistent with the (220) and (440) lattice planes. The (220) plane is also observed from the HRTEM of CO/ZCO (3.5mmol, 12h, 2), the smaller hollow spheres, and the selected area electron diffraction (SAED) pattern indicates a polycrystalline structure, Figure 4(d). The distribution maps of Co and Zn in the larger sphere of CO/ZCO (1.3mmol, 12h, 10), figures 4(e, f), and the line scan mapping show clear maxima for Co and O at the edge of the particle, figures 4(g), confirming that the large spheres are hollow. Line scan mapping of the smaller spheres of CO/ZCO (3.5mmol, 12h, 2), Figure S12a show maxima for Zn, Co and O at the edge of the particles, consistent with hollow spheres being formed. Both line scans show a Zn content less than half that of the Co supporting formation of a $ZnCo_2O_4/Co_3O_4$ composite on pyrolysis of the MOFs, in agreement with the XPS and ICP analysis. However, CO/ZCO (3.5mmol, 12h, 2, 550C-0hAr-350C-2hAir) with a high content of Zn shows non-hollow spheres in TEM (Figure 4h) and an increased concentration of Zn in the sphere middle compared with low-temperature pyrolysis compound, CO/ZCO (3.5mmol, 12h, 2, 350C-2hAir), see the line mapping of the elements in Figure S12b and c, indicating the process of Zn loss is key to the formation of the hollow sphere.

The hollow structure is proposed to form via a thermal vapor mechanism (Figure 4i) by evaporating the molten Zn from the center of the pyrolysed particle, which is consistent with the analysis of the XRD results. (I) The pyrolysis of ZnCo MOFs in Ar at 550 ^{o}C produces particles composed of ZnO and Co nanoparticles of spherical shape because the self-templated growth of the MOF tends to start form an initial spherical nanoparticle[41]. (II) ZnO is condensed to the center of

the pyrolyzed particle and reduced to Zn within the reducing environment involving carbon and Co nanoparticles. (III) The continuous annealing at 550 ^{o}C in Ar results in Zn melting and (IV) evaporation via the thermal vapor leaving the hollow core. Co particles are oxidized by the air at 350 ^{o}C to Co_3O_4 and react with remaining ZnO to form $ZnCo_2O_4$. In this process, the nanoscale Kirkendall effect, as a result of the non-equal net flow of matter between Co core and Co_3O_4 shell, also contributes to the formation of hollow core[42-45].The hollow Co_3O_4 shell structure is doped with $ZnCo_2O_4$ the amount of which is tunable through controlling the Zn loss in step (III).

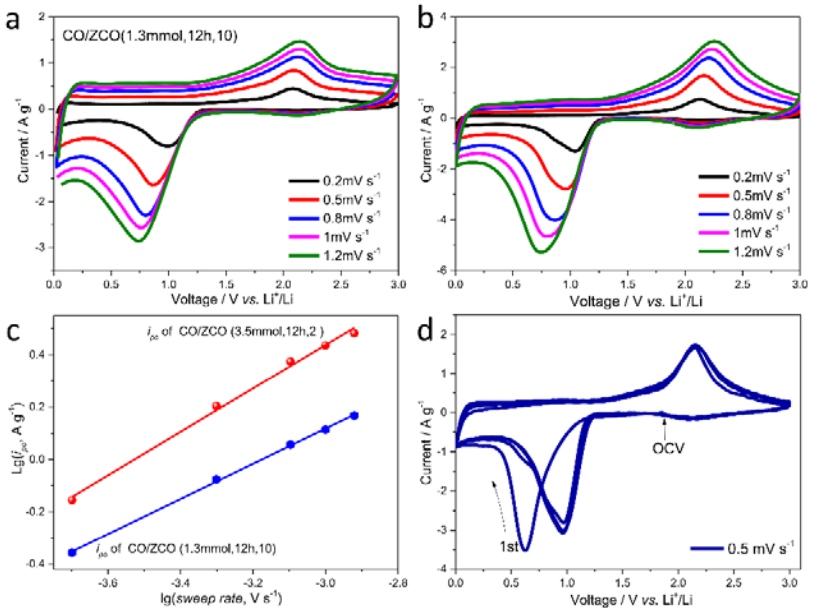

Figure 5. Cyclic voltammetry of (a) CO/ZCO (1.3mmol, 12h, 10) and (b) CO/ZCO (3.5mmol, 12h, 2). (c) The linear fitting of lg(oxidative peak current) to lg(sweep rate) from the curves in (a) and (b). (d) First five cyclic voltammograms of CO/ZCO (3.5mmol, 12h, 2) at a scan rate of 0.5 mV s^{-1}.

Cyclic voltammograms of LIBs with CO/ZCO (1.3mmol, 12h, 10) and CO/ZCO (3.5mmol, 12h, 2) anodes were recorded across a range of scan rates from 0.2 to 1.2 mV s^{-1}, **Figure 5**(a-b). The anodic and cathodic peaks shift slightly with increasing scan rates for both samples, indicating low electrode polarization and good reversibility in the electrochemical reaction. Considering the relationship

between the peak current and scan rate, $i=av^b$, the b values can be calculated using the lg(v)-lg(i) plot, where a b value of unity indicates capacitive (pseudocapacitive) behavior and a b of 0.5 signifies a diffusion limited reaction[46, 47]. The linear plots in Figure 5c presents the slope between lg(oxidative peak current) and lg(sweep rate) of CO/ZCO (1.3mmol, 12h, 10) to be 0.67 and CO/ZCO (3.5mmol, 12h, 2) 0.83. The slope of 0.67 approaches the diffusion-controlled process and that of 0.83 means a tendency for a surface-controlled mechanism. The control step for the electrochemistry of CO/ZCO changes from diffusion-control to surface-control by tuning the particle size from hundreds to tens of nanometers, see SEM and TEM images. The nano-sized particles are too small to provide diffusion channels and the electrochemical reaction dominates on the sample surface. To understand the electrochemical insertion/deinsertion reaction of lithium ions into the sample, potentiostatic CV at 0.5 mV s^{-1} was carried out on CO/ZCO (3.5mmol, 12h, 2) and the first five cycles are displayed in Figure 5d. In the first cycle, starting from the open circuit voltage of 1.8 V, there is one abrupt but irreversible cathodic peak at 0.6 V, assigned to the multi-step lithium insertion and electrolyte decomposition reaction[6, 13, 48]. From the second CV cycle, only one pair of redox peaks, 0.95 V for cathodic and 2.2 V for anodic present in the voltammograms, signifying the conversion reaction between Co_3O_4 and Co as follow[49]:

$$Co_3O_4 + 8Li^+ + 8e^- \leftrightarrow 3Co + 4Li_2O \qquad (1)$$

In comparison with the first cycle, the cathodic peaks of the subsequent cycles have slightly smaller current, while anodic peaks display similar current throughout, confirming the occurrence of an irreversible reaction in the first cycle by forming solid electrolyte interface (SEI). The cathodic peaks are still sharp with small full width at half maximum, which is different from the broad peaks reported for Co_3O_4 but similar to the voltammograms of $ZnCo_2O_4$[50]. The broad cathodic peaks partially result from the formation of the SEI layer[13] which consumes a large amount of charges while the sharp peaks of CO/ZCO (3.5mmol, 12h, 2) imply a small loss of charge in SEI after the first cycle and this result is attributed to the mature SEI layer formed in the first cycle which can be due to the synergistic

effect from the dopant, $ZnCo_2O_4$. The following four cycles almost overlapp the CV curves, indicating excellent reversibility of the electrode.

Table 1. The specific capacity in mAh g^{-1} of CO/ZCO samples working at current rates ranging from 0.1 to 10 A g^{-1}.

CO/ZCO samples	0.1A g^{-1}	0.2A g^{-1}	0.5A g^{-1}	1A g^{-1}	2A g^{-1}	5A g^{-1}	10A g^{-1}
CO/ZCO(1.3mmol, 12h, 10)	707	680	612	555	476	358	243
CO/ZCO(3.5mmol,12h, 10)	764	753	708	633	556	426	302
CO/ZCO(3.5mmol,12h, 2)	890	888	853	822	787	705	621
CO/ZCO(3.5mmol,16h, 2)	683	682	657	608	540	437	354
CO/ZCO(3.5mmol,12h, 2, 550C-0hAr-350C-2hAir)	921	891	833	786	714	476	217
CO/ZCO(3.5mmol,12h,2, 350C-2hAir)	922	771	616	468	291	85	35

Table 2 Comparison of the lithium-ion storage properties with published work.

Sample	Specific capacity/ mAh g^{-1}	Degradation in each cycle
Hollow Co_3O_4	880@0.05 A g^{-1}	1.1 mAh g^{-1}@0.1 A g^{-1}[51]
Quaduple-shelled Co_3O_4	1626@0.05 A g^{-1}	20.5 mAh g^{-1}@0.05 A g^{-1}[52]
Co_3O_4 platelets	700@0.1 A g^{-1}	1 mAh g^{-1}@0.1 A g^{-1}[53]
Mesoporous Co_3O_4 nanoplates	1400@0.45 A g^{-1}	2.9 mAh g^{-1}@0.45 A g^{-1}[54]
Co_3O_4 hexapods	1100@0.1 A g^{-1}	7.5 mAh g^{-1}@0.1 A g^{-1}[55]
Co_3O_4 nanotube	1200@0.05 A g^{-1}	10 mAh g^{-1}@0.05 A g^{-1}[56]
Co_3O_4 pyrolyzed from ZIF67	1040@0.1 A g^{-1}	0.82 mAh g^{-1}@0.2 A g^{-1}[57]
Porous Co_3O_4 nanosheets	1450@0.05 A g^{-1}	1.6 mAh g^{-1}@0.05 A g^{-1}[58]
Mesoporous Co_3O_4 nanobundles	14680@0.1 A g^{-1}	2 mAh g^{-1}@0.05 A g^{-1}[59]
rGO@Co_3O_4	1451@0.1 A g^{-1}	5.8 mAh g^{-1}@0.1 A g^{-1}[60]
CO/ZCO (this work)	822@1 A g^{-1}	0.76 mAh g^{-1}@2 A g^{-1}

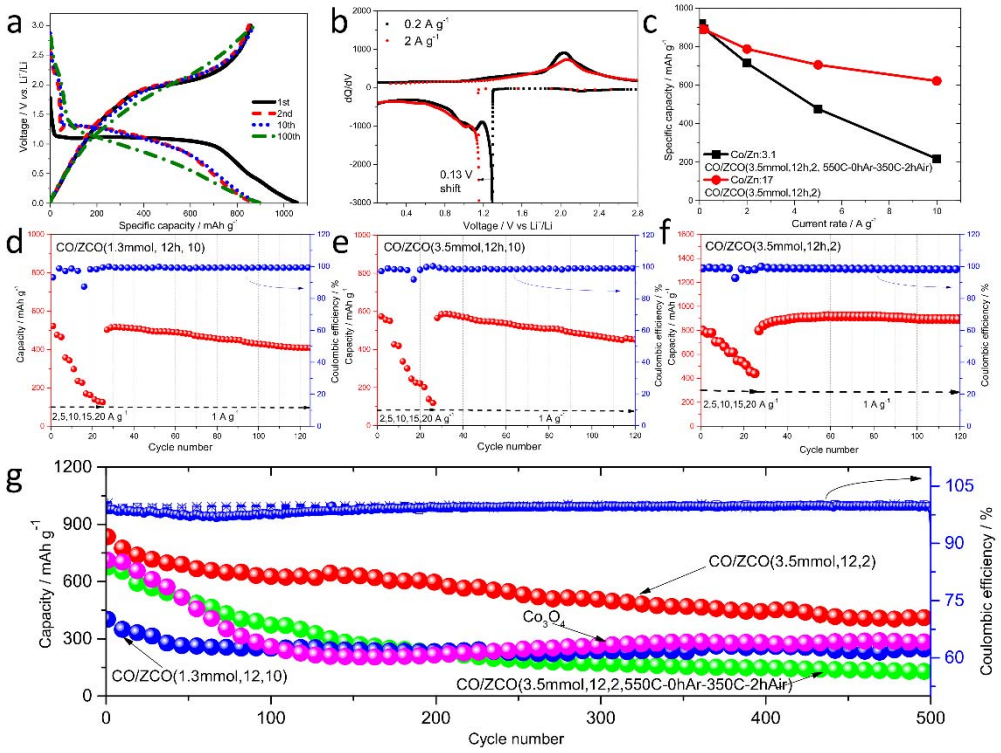

Figure 6. Galvanostatic charge/discharge performance. (a) Voltage profiles of CO/ZCO (3.5mmol, 12h, 2) of the 1st, 2nd, 10th and 100th cycle at 0.1 A g^{-1}. (b) Relation between capacity differential and voltage of CO/ZCO (3.5mmol,

12h, 2) at 0.2 and 2 A g^{-1}. (c) Comparison in the specific capacity of CO/ZCO (3.5mmol, 12h, 2, 550-0hAr-350-2hAir) and CO/ZCO (3.5mmol, 12h, 2) with different Co/Zn ratios of 3.1 and 17. The cycling performance at different current rates of 2, 5, 10, 15, 20 and then 1 A g^{-1} of (d) CO/ZCO (1.3mmol, 12h, 10), (e) CO/ZCO (3.5mmol, 12h, 10) and (f) CO/ZCO (3.5mmol, 12h, 2). (g) The long-term cycling performance of CO/ZCO (3.5mmol, 12h, 2) compared with CO/ZCO (1.3mmol, 12h, 10) large hollow sphere, CO/ZCO (3.5mmol, 12h, 2, 550C-0hAr-350C-2hAir) and Co_3O_4 pyrolysed from the Co-MOF at 2 A g^{-1}.

The galvanostatic charge/discharge performance of batteries prepared using as-synthesised CO/ZCO composites as anodes are shown in **Figure 6** and S13 and the specific capacities of the samples measured at current densities ranging from 0.1 to 10 A g^{-1} are listed in **Table 1**. Voltage profiles of CO/ZCO (3.5mmol, 12h, 2) of the 1st, 2nd, 10th and 100th cycle at 0.1 A g^{-1} are displayed in Figure 6a. In the first discharge profile, there is one plateau and one slope for the lithium reaction below ~1.2 V while in the subsequent cycles, the plateau dimishes and a single slope is observed, a behavior of a solid solution reaction[61] from Co^{3+} and Co^0. The initial discharge and charge capacities are 1051 and 858 mA h g^{-1} respectively, corresponding to a high coulombic efficiency of 81.6 %. The profile of capacity differential versus voltage of CO/ZCO (3.5mmol, 12h, 2) at 0.2 and 2 A g^{-1} dispalys a potential shift of 0.13 V in the reduction reaction and this small shift in overpotential when the current density increases by then times imply the high rate capability. All cells show appreciable capacities at low current densities and the samples with high content of Zn, CO/ZCO(3.5mmol, 12h, 2, 550C-0hAr-350C-2hAir) and CO/ZCO(3.5mmol, 12h, 2, 350C-2hAir) in the anode material display the highest capacity at 0.1 A g^{-1}, resulting from the residue ZnO and doped $ZnCo_2O_4$ which possess high theoretical capacity. Remarkably CO/ZCO

(3.5mmol,12h,2) maintains a high capacity at increased current densities, the capacity decreasing by only 30% when the cell operates at a current of 10 A g^{-1}, see Figure 6a. Similarly in the cell containing CO/ZCO (3.5mmol,16h,2) the capacity falls by only 48% when the current density is increased from 0.1 A g^{-1} to 10 A g^{-1}. In contrast cells containing CO/ZCO formed at a higher heating rate of 10 ^{o}C min^{-1} during pyrolysis show a fall in the capacity of 66%. Worse are the CO/ZCO (3.5mmol,12h, 2, 550-0hAr-350-2hAir) and CO/ZCO (3.5mmol,12h, 2, 350-2hAir) samples which both contain a high atomic ratio of Zn and show capacity drops of 76.4 and 96.2%, respectively. To further investigate whether the low pyrolysis heating rate, 2 ^{o}C min^{-1} which lead to the parent MOF structure being maintained and small hollow spheres of CO/ZCO, minimizes material degradation on cycling, experiments were performed at very high current densities. The capacity was monitored as the cell was continuously cycled at different current densities, 2, 5, 10, 15 and 20 A g^{-1} (5 cycles each) and 1 A g^{-1} (100 cycles). Cells containing CO/ZCO(1.3mmol, 12h, 10) and CO/ZCO(3.5mmol, 12h, 10) both show noticeable decreases in performance at high current densities and appreciable decreases in capacity as the cells are continuously cycled at 1 A g^{-1} following the high-rates cycling, see Figure 6(b, c). In contrast, the cells containing CO/ZCO (3.5mmol, 12h, 2) in Figure 6d show much higher capacities and better stablility when cycled at 1 A g^{-1}.

It is of note that for cells containing CO/ZCO (3.5mmol, 12h, 2) the capacity measured at 1 A g^{-1} post high current cycling, 890 mAh g^{-1}, is greater than that measured at the same current prior to any high current cycling, 822 mAh g^{-1}. This suggests the electrode and electrode/electrolyte interface within the nanospherical hollow structures are activated during lithiation/delithiation at high current densities. The long-term cycling performance of cells containing CO/ZCO (3.5mmol, 12h, 2), CO/ZCO (1.3mmol, 12h, 10), CO/ZCO (3.5mmol, 12h, 2, 550C-0hAr-350C-2hAir) and Co_3O_4 at 2 A g^{-1} in Figure 6e shows that

CO/ZCO (3.5mmol, 12h, 2) keeps the highest retained capacity of 409 mAh g^{-1} (0.76 mAh g^{-1} drop each cycle) after 500 cycles. The almost 100% coulombic efficiency during the cycling demonstrates good reversibility of lithiation/delithiation of the composite electrode, suggesting the superior structure of strips surrounded with nanospheres and a small amount of ZCO dopant of CO/ZCO (3.5mmol, 12h, 2) significantly improve the lithium ion storage properties. In comparison, the high amount of ZCO dopant in CO/ZCO (3.5mmol, 12h, 2, 550C-0hAr-350C-2hAir) and non-hollow structure of Co_3O_4 - cause serious degradation in the capacity. CO/ZCO (1.3mmol, 12h, 10) in hollow microspheres exhibits a capacity retaintion of 40% after 500 cycles at 2 A g^{-1} and lower specific capacity than CO/ZCO (3.5mmol, 12h, 2). The excellent cycling properties of CO/ZCO (3.5mmol, 12h, 2) is much better than the reported results, see Table 2. A number of reported specific capacities even after the initial cycle are still greatly larger than the theoretical capacity of Co_3O_4, 890 mAh g^{-1} mainly attributed to the eletrolyte decomposition[62]. Co_3O_4 from the direct pyrolysis of ZIF-67[57] shows 1.48 mAh g^{-1} drop each cycle at 0.1 A g^{-1} and only around 250 mAh g^{-1} at 2 A g^{-1}. Needle-like Co_3O_4 nanotubes[56] display 6.83 mAh g^{-1} drop each cycle at 0.05 A g^{-1}. The nanocomposite of Co_3O_4 nanoparticles anchored on reduced graphene oxide[13] display a specific capacity of around 400 mAh g^{-1} at 0.5 A g^{-1} after 40cycles. The SEM images of CO/ZCO (1.3mmol, 12h, 10) and CO/ZCO (3.5mmol, 12h, 2) after the long-term cycling are shown in Figure S14. The morphological spheres of both samples are well maintained and CO/ZCO (3.5mmol, 12h, 2) displays clear separate spheres although the microspheres of CO/ZCO (1.3mmol, 12h, 10) tend to agglomerate indicating the strong structural statability.

To investigate the initial stages of degradation in cells containing CO/ZCO (3.5mmol, 12h, 2) the delta differential capacity, $\Delta dQ/dV$[63, 64], was measured for the first five cycles at 100 mA g^{-1} in Figure S15. In the cathodic

range the materials show a distinct change in peak potential between the first cycle and subsequent cycles, with the peak changing in position by 250 mV. In the anodic scan there are peaks at 2.0 V and 1.5 V. The cathodic peak is consistent with the reduction of Co_3O_4 and $ZnCo_2O_4$ to metallic cobalt and zinc respectively and the formation of Li_2O[6, 65]. There is no extra peak denoting the Zn alloying reaction resulting form the low content of $ZnCo_2O_4$ dopant in the composite. The shift in the cathodic peak position in subsequent cycles has been assigned to the growth of solid electrolyte interphase (SEI) films. The high potential peak in the anodic scan matches the oxidation of Co whilst the low potential anodic peak fits the zinc oxidation peak observed in cyclic voltammetric studies of $ZnCo_2O_4$[65].

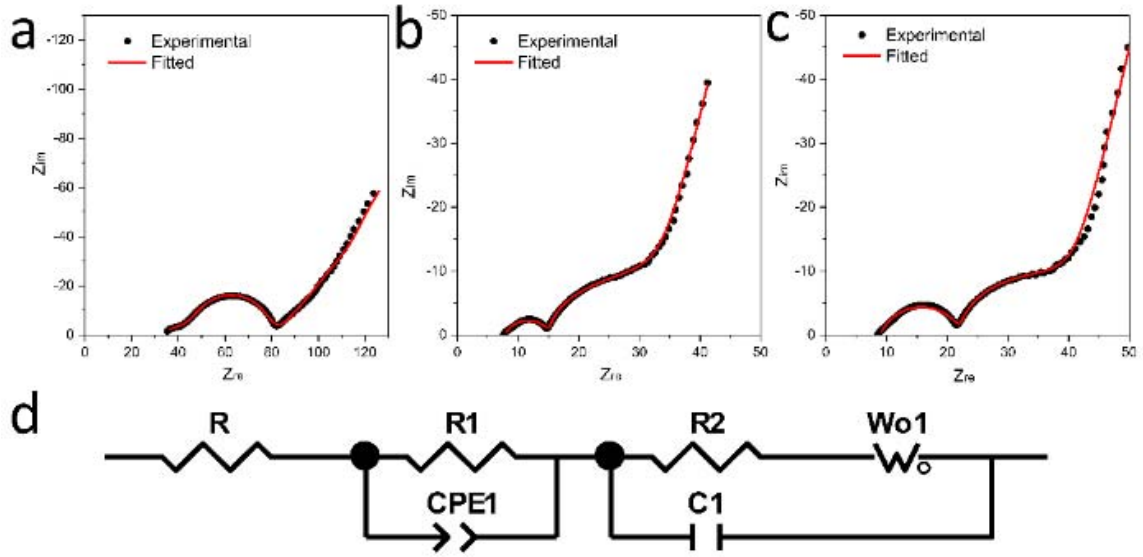

Figure 7 EIS analysis of the samples after 120 cycles. Nyquist plot of (a) CO/ZCO (1.3mmol, 12h, 10), (b) CO/ZCO (3.5mmol, 12h, 2), (c) CO/ZCO (3.5mmol, 16h, 2). (d) Equivalent circuit used for data fitting.

Electrochemical impedance spectroscopy (EIS) was used to study the kinetic parameters of the as-prepared CO/ZCO composite electrode in LiBs. **Figures 7**(a-c) show the Nyquist plots of CO/ZCO (1.3mmol, 12h, 10), CO/ZCO (3.5mmol, 12h, 2) and CO/ZCO (3.5mmol, 16h, 2) after 120 cycles and their

corresponding fitted plots which are calculated from the equivalent circuit model in Figure 7d. The values with errors of each component in the equivalent circuit are listed in Table S3. In the equivalent circuit model, R represents the internal resistance of the cell and mainly arises from the electrode and electrolyte. R1 and CPE1 (constant phase element) are the resistance and pseudocapacitance generated on the porous surface of the electrode[66], signifying the first semi-circle at high frequency. R2 represents the charge transfer resistance and C1 is the capacitor in the bulk associated with Li^+ ions insertion, giving rise to second semi-circle at intermediate frequency. The slope in the low frequency denotes the Warburg resistance resulting from the solid-state ion diffusion in the electrode. The values of R, R1 and R2 of CO/ZCO (3.5mmol, 12h, 2) and CO/ZCO (3.5mmol, 16h, 2) are smaller than CO/ZCO (1.3mmol, 12h, 10) while C1 is larger, indicating the small particle size benefits the connection (**Figure 8**a) thus high conductivity, and enhances the capacitive storage, in good agreement with the kinetic analysis in the CV part. The Warburg component shows open-circuit characteristics, e.g., a tendency to be vertical in the Nyquist plot at low frequency range[67], resulting from the reflective boundary for the finite diffusion, as depicted in Figure 8b. Moreover, considering the inverse proportion relationship between the diffusion coefficient[47, 48, 68], D and the Warburg factor, σ which is calculated from the function of Z_{re} *vs.* $\omega^{-1/2}$ in Figure S16, the two samples, CO/ZCO (3.5mmol, 12h, 2) and CO/ZCO (3.5mmol, 16h, 2) with smaller particle sizes are deduced to have much faster diffusion rate than CO/ZCO (1.3mmol, 12h, 10). The nanosizing particle shortens the diffusion pathway and provides abundant channels for electrolyte penetration thus has faster diffusion and larger capacitance at high frequency[1, 69-71], as shown in Figure 8c.

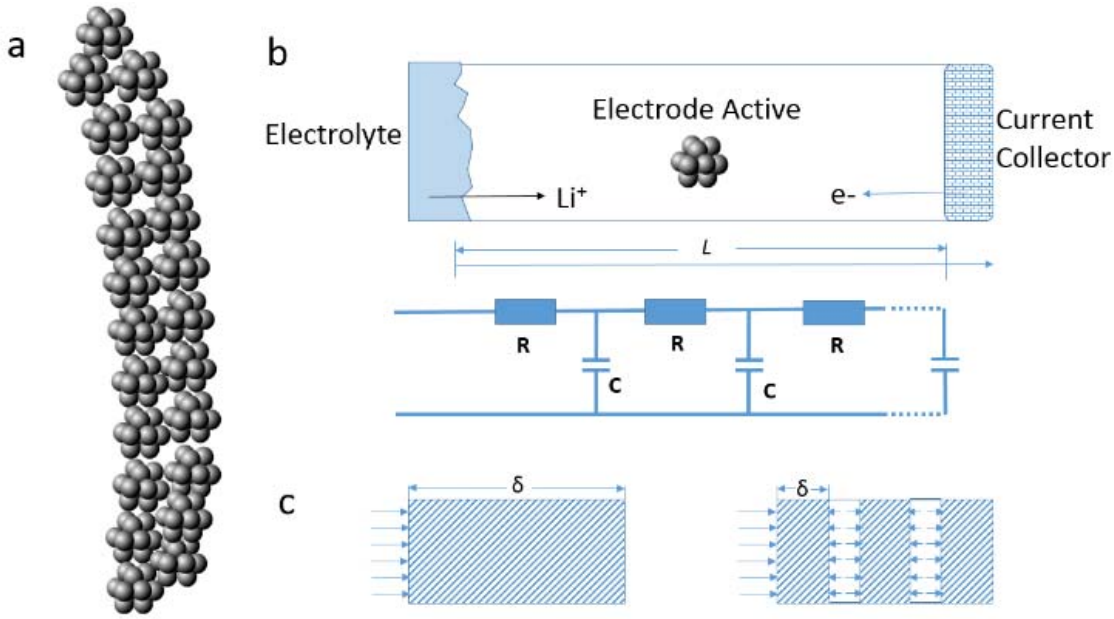

Figure 8 Schematic representation of the prepared hollow-nanosphere aggregated structure arranged in a stripe (a). (b) The insertion reaction of Li ions into the electrode and transmission line equivalent circuit with an open-circuit terminal within the finite length, L. (c) Scheme of solid-state diffusion and formed capacitance in terms of the layer thickness, δ of the electrode.

4. Conclusions

Hollow Co_3O_4 spheres doped with $ZnCo_2O_4$ via the pyrolysis of the Zn/Co mixed-ion metal organic frameworks (MOFs) were prepared as anode materials in lithium-ion batteries. The hollow structure is formed via the thermal vapor of Zn by reducing ZnO at temperatures above the melting point of Zn. The doped binary metal oxide acts to both improve the conductivity and store lithium ions. The amount of dopant is controlled by the pyrolysis condition. Nanospheres arranged in strips by decomposing ZnCoMOF (3.5mmol, 12h) at a slow rate, 2 $^{o}C\ min^{-1}$, present the best performance as anodes in the lithium ion batteries. They display a specific capacity of 890 mAh g^{-1} at a current rate of 0.1 A g^{-1} and show a similar specific capacity of 890 mAh g^{-1} at 1 A g^{-1} after 120 cycles at high current densities. The nanosized particles

are capable of shortening the diffusion pathway and providing abundant channels for electrolyte penetration leading to faster diffusion and the larger capacity at large frequency. The thermal vapor route has potential to derive other transition metal oxides doped with the zinc-based binary metal oxides to form hollow structure.

Supporting Information. More characterization and electrochemical test results.

Acknowledgement

We thank the President's Ph.D. Scholarship of Imperial College London, the Engineering and Physical Sciences Research Council (EPSRC, Grant: EP/L015277/1) and STFC Futures Early Career Award (2016) for financial support. The Authors acknowledge use of characterisation facilities within the Harvey Flower Electron Microscopy Suite, Department of Materials, Imperial College London.

References

[1] N. Mahmood, T.Y. Tang, Y.L. Hou, Adv. Energy Mater., 6 (2016) 1600374.

[2] M. Armand, J.M. Tarascon, Nature, 451 (2008) 652-657.

[3] S.W. Lee, N. Yabuuchi, B.M. Gallant, S. Chen, B.-S. Kim, P.T. Hammond, Y. Shao-Horn, Nat. Nanotech., 5 (2010) 531-537.

[4] W. Qi, J.G. Shapter, Q. Wu, T. Yin, G. Gao, D. Cui, J. Mater. Chem. A, 5 (2017) 19521-19540.

[5] P. Roy, S.K. Srivastava, J. Mater. Chem. A, 3 (2015) 2454-2484.

[6] X. Leng, S. Wei, Z. Jiang, J. Lian, G. Wang, Q. Jiang, Sci. Rep., 5 (2015) 16629.

[7] X. Xu, K. Cao, Y. Wang, L. Jiao, J. Mater. Chem. A, 4 (2016) 6042-6047.

[8] C. Yuan, H.B. Wu, Y. Xie, X.W. Lou, Angew. Chem., Int. Ed., 53 (2014) 1488-1504.

[9] Y. Zheng, T. Zhou, X. Zhao, W.K. Pang, H. Gao, S. Li, Z. Zhou, H. Liu, Z. Guo, Adv. Mater., 29 (2017) 1700396.

[10] Y. Li, B. Tan, Y. Wu, Nano Lett., 8 (2008) 265-270.

[11] W. Song, R. Brugge, I.G. Theodorou, A.L. Lim, Y. Yang, T. Zhao, C.H. Burgess, I.D. Johnson, A. Aguadero, P.R. Shearing, D.J.L. Brett, F. Xie, D.J. Riley, ACS Appl. Mater. Interfaces, 9 (2017) 37823-37831.

[12] W. Liu, T. Zhou, Y. Zheng, J. Liu, C. Feng, Y. Shen, Y. Huang, Z. Guo, ACS Appl. Mater. Interfaces, 9 (2017) 9778-9784.

[13] Z.-S. Wu, W. Ren, L. Wen, L. Gao, J. Zhao, Z. Chen, G. Zhou, F. Li, H.-M. Cheng, ACS Nano, 4 (2010) 3187-3194.

[14] L. Li, G. Zhou, X.-Y. Shan, S. Pei, F. Li, H.-M. Cheng, J. Power Sources, 255 (2014) 52-58.

[15] D. Li, H. Wang, T. Zhou, W. Zhang, H.K. Liu, Z. Guo, Adv. Energy Mater., 7 (2017) 1700488.
[16] L. Yu, H. Hu, H.B. Wu, X.W. Lou, Adv. Mater., 29 (2017) 1604563.
[17] J. Liu, N.P. Wickramaratne, S.Z. Qiao, M. Jaroniec, Nat. Mater., 14 (2015) 763.
[18] J. Liu, T. Yang, D.-W. Wang, G.Q. Lu, D. Zhao, S.Z. Qiao, Nat. Commun., 4 (2013) 2798.
[19] H. Tian, H. Liu, T. Yang, J.-P. Veder, G. Wang, M. Hu, S. Wang, M. Jaroniec, J. Liu, Materials Chemistry Frontiers, 1 (2017) 823-830.
[20] L. Hu, B. Qu, C. Li, Y. Chen, L. Mei, D. Lei, L. Chen, Q. Li, T. Wang, J. Mater. Chem. A, 1 (2013) 5596-5602.
[21] G. Gao, H.B. Wu, B. Dong, S. Ding, X.W. Lou, Advanced Science, 2 (2015) 1400014.
[22] W.-T. Koo, H.-Y. Jang, C. Kim, J.-W. Jung, J.Y. Cheong, I.-D. Kim, J. Mater. Chem. A, 5 (2017) 22717-22725.
[23] R. Chen, Y. Hu, Z. Shen, Y. Chen, X. He, X. Zhang, Y. Zhang, ACS Appl. Mater. Interfaces, 8 (2016) 2591-2599.
[24] H.B. Wu, B.Y. Xia, L. Yu, X.Y. Yu, X.W. Lou, Nat. Commun., 6 (2015) 6512.
[25] F. Zou, X. Hu, Z. Li, L. Qie, C. Hu, R. Zeng, Y. Jiang, Y. Huang, Adv. Mater., 26 (2014) 6622-6628.
[26] S.J. Yang, S. Nam, T. Kim, J.H. Im, H. Jung, J.H. Kang, S. Wi, B. Park, C.R. Park, J. Am. Chem. Soc., 135 (2013) 7394-7397.
[27] G. Zou, H. Hou, P. Ge, Z. Huang, G. Zhao, D. Yin, X. Ji, Small, 14 (2018).
[28] G. Zou, H. Hou, X. Cao, P. Ge, G. Zhao, D. Yin, X. Ji, J. Mater. Chem. A, 5 (2017) 23550-23558.
[29] H. Tian, S. Wang, C. Zhang, J.-P. Veder, J. Pan, M. Jaroniec, L. Wang, J. Liu, J. Mater. Chem. A, 5 (2017) 11615-11622.
[30] I. Luz, A. Loiudice, D.T. Sun, W.L. Queen, R. Buonsanti, Chem. Mater., 28 (2016) 3839-3849.
[31] S. Yuan, T.-F. Liu, D. Feng, J. Tian, K. Wang, J. Qin, Q. Zhang, Y.-P. Chen, M. Bosch, L. Zou, S.J. Teat, S.J. Dalgarno, H.-C. Zhou, Chem. Sci., 6 (2015) 3926-3930.
[32] R. Berenguer, T. Valdés-Solís, A. Fuertes, C. Quijada, E. Morallon, J. Electrochem. Soc., 155 (2008) K110-K115.
[33] C.C. Wang, M. Liu, B.Y. Man, C.S. Chen, S.Z. Jiang, S.Y. Yang, X.G. Gao, S.C. Xu, B. Hu, Z.C. Sun, J.J. Guo, J. Hou, AIP Advances, 2 (2012) 012182.
[34] M.H. Huang, Y. Wu, H. Feick, N. Tran, E. Weber, P. Yang, Adv. Mater., 13 (2001) 113-116.
[35] X.B. Du, H. Lv, D.D. Sang, H.D. Li, D.M. Li, G.T. Zou, Nanoscale Research Letters, 5 (2010) 620-624.
[36] H.-D. Li, H. Lü, D.-D. Sang, D.-M. Li, B. Li, X.-Y. Lü, G.-T. Zou, Chinese. Phys. Lett., 25 (2008) 3794-3797.
[37] L. Wang, K. Chen, Cryst. Res. Technol., 48 (2013) 163-168.
[38] L. Oar-Arteta, T. Wezendonk, X. Sun, F. Kapteijn, J. Gascon, Materials Chemistry Frontiers, 1 (2017) 1709-1745.
[39] H.J.T. Ellingham, J. Soc. Chem. Ind. (J. Chem. Technol. Biotechnol.), 10 (1944) 125-133.
[40] N.H. Perry, T.O. Mason, C. Ma, A. Navrotsky, Y. Shi, J.S. Bettinger, M.F. Toney, T.R. Paudel, S. Lany, A. Zunger, J. Solid State Chem., 190 (2012) 143-149.
[41] I. Lee, S. Choi, H.J. Lee, M. Oh, Cryst. Growth Des., 15 (2015) 5169-5173.
[42] L. Gao, C. Pang, D. He, L. Shen, A. Gupta, N. Bao, Sci. Rep., 5 (2015) 16061.
[43] C. Guan, A. Sumboja, H. Wu, W. Ren, X. Liu, H. Zhang, Z. Liu, C. Cheng, S.J. Pennycook, J. Wang, Adv. Mater., 29 (2017) 1704117.
[44] Y.-E. Miao, F. Li, Y. Zhou, F. Lai, H. Lu, T. Liu, Nanoscale, 9 (2017) 16313-16320.
[45] W. Wang, M. Dahl, Y. Yin, Chem. Mater., 25 (2013) 1179-1189.

[46] C. Chen, Y. Wen, X. Hu, X. Ji, M. Yan, L. Mai, P. Hu, B. Shan, Y. Huang, Nat. Commun., 6 (2015) 6929.
[47] W. Song, X. Ji, Z. Wu, Y. Zhu, Y. Yao, K. Huangfu, Q. Chen, C.E. Banks, J. Mater. Chem. A, 2 (2014) 2571-2577.
[48] X.L. Wu, Y.G. Guo, J. Su, J.W. Xiong, Y.L. Zhang, L.J. Wan, Adv. Energy Mater., 3 (2013) 1155-1160.
[49] H. Yu, H. Fan, X. Wu, H. Wang, Z. Luo, H. Tan, B. Yadian, Y. Huang, Q. Yan, Energy Storage Materials, 4 (2016) 145-153.
[50] J. Deng, X. Yu, X. Qin, B. Liu, Y.-B. He, B. Li, F. Kang, Energy Storage Materials, 11 (2018) 184-190.
[51] D. Wang, Y. Yu, H. He, J. Wang, W. Zhou, H.D. Abruña, ACS Nano, 9 (2015) 1775-1781.
[52] J. Wang, N. Yang, H. Tang, Z. Dong, Q. Jin, M. Yang, D. Kisailus, H. Zhao, Z. Tang, D. Wang, Angew. Chem., Int. Ed., 52 (2013) 6417-6420.
[53] W. Yao, J. Yang, J. Wang, Y. Nuli, J. Electrochem. Soc., 155 (2008) A903-A908.
[54] D. Su, X. Xie, P. Munroe, S. Dou, G. Wang, Sci. Rep., 4 (2014) 6519.
[55] L. Wang, B. Liu, S. Ran, H. Huang, X. Wang, B. Liang, D. Chen, G. Shen, J. Mater. Chem., 22 (2012) 23541-23546.
[56] X.W. Lou, D. Deng, J.Y. Lee, J. Feng, L.A. Archer, Adv. Mater., 20 (2008) 258-262.
[57] Q. Qu, T. Gao, H. Zheng, X. Li, H. Liu, M. Shen, J. Shao, H. Zheng, Carbon, 92 (2015) 119-125.
[58] F. Zhan, B. Geng, Y. Guo, Chem – Eur J, 15 (2009) 6169-6174.
[59] Y. Xiao, C. Hu, M. Cao, J. Power Sources, 247 (2014) 49-56.
[60] D. Yin, G. Huang, Q. Sun, Q. Li, X. Wang, D. Yuan, C. Wang, L. Wang, Electrochim. Acta, 215 (2016) 410-419.
[61] W.K. Pang, V.K. Peterson, N. Sharma, C. Zhang, Z. Guo, J. Phys. Chem. C, 118 (2014) 3976-3983.
[62] H. Chen, Q. Zhang, J. Wang, D. Xu, X. Li, Y. Yang, K. Zhang, J. Mater. Chem. A, 2 (2014) 8483-8490.
[63] A.J. Smith, J.R. Dahn, J. Electrochem. Soc., 159 (2012) A290-A293.
[64] A.J. Smith, J.C. Burns, J.R. Dahn, Electrochem. Solid St., 14 (2011) A39-A41.
[65] W. Luo, X. Hu, Y. Sun, Y. Huang, J. Mater. Chem., 22 (2012) 8916-8921.
[66] Q.L. Wu, J.G. Xu, X.F. Yang, F.Q. Lu, S.M. He, J.L. Yang, H.J. Fan, M.M. Wu, Adv. Energy Mater., 5 (2015) 1401756.
[67] Q. Wang, W. Zhang, C. Guo, Y. Liu, C. Wang, Z. Guo, Adv. Funct. Mater., 27 (2017) 1703390.
[68] W. Song, X. Ji, Z. Wu, Y. Yang, Z. Zhou, F. Li, Q. Chen, C.E. Banks, J. Power Sources, 256 (2014) 258-263.
[69] G. Xia, L. Zhang, F. Fang, D. Sun, Z. Guo, H. Liu, X. Yu, Adv. Funct. Mater., 26 (2016) 6188-6196.
[70] F. Cheng, W.-C. Li, J.-N. Zhu, W.-P. Zhang, A.-H. Lu, Nano Energy, 19 (2016) 486-494.
[71] Q. Mahmood, S.K. Park, K.D. Kwon, S.-J. Chang, J.-Y. Hong, G. Shen, Y.M. Jung, T.J. Park, S.W. Khang, W.S. Kim, J. Kong, H.S. Park, Adv. Energy Mater., 6 (2016) 1501115.